



Simulations of hindered settling of flocculating spherical particles



J.J. Derksen*

Chemical & Materials Engineering, University of Alberta, Edmonton, Alberta T6G 2G6, Canada
School of Engineering, University of Aberdeen, Aberdeen, AB24 3UE Scotland, UK

ARTICLE INFO

Article history:

Received 21 June 2013

Received in revised form 1 September 2013

Accepted 5 September 2013

Available online 17 September 2013

Keywords:

Solid–liquid flow

Sedimentation

Aggregation

Flocculation

Lattice-Boltzmann method

Square-well potential

ABSTRACT

Direct simulations of solid particles settling in a Newtonian liquid have been performed. The particles were given an attractive interaction potential of a square-well shape which made them aggregate and – as a result – settle faster. The lattice-Boltzmann method was used to solve the liquid flow in between the uniformly sized spherical particles. An immersed boundary method was applied to impose no-slip at the surfaces of the spheres that are free to move and rotate under the influence of net gravity, hydrodynamic forces, collisions and the interaction potential. Solids volume fractions were in the range 0.12–0.32, and Reynolds numbers (based on average superficial slip velocity) went up to order 50. Drag reduction due to aggregation has been correlated with average aggregate size. This correlation is a strong function of Reynolds number and solids volume fraction.

© 2013 Elsevier Ltd. All rights reserved.

1. Introduction

Solid particles settling in liquid under the influence of gravity is a topic of research with a long and rich tradition (Stokes, 1901; Richardson and Zaki, 1954a, 1954b; Batchelor, 1972), continuing interest (Ladd, 2002; Mucha et al., 2004; Nguyen and Ladd, 2005; Guazzelli and Hinch, 2011), and significant practical relevance. The latter not only because of its application for gravity-based separation, but also in view of fluidization which is a common operation for a variety of industrial processes involving fluid–solid contacting and mixing. For small particles settling in liquids with high viscosities, settling rates get very low which is not good for achieving high process efficiency. One way to enhance settling rates is to promote aggregation (“flocculation”) of the particles so that they form aggregates that fall faster through the liquid. Flocculation is usually triggered by adding chemicals (flocculants) to the solid–liquid suspension. For instance, polymeric flocculants (Wang et al., 2010) with an affinity for solid–liquid interfaces promote the formation of bridges connecting particles. In fluidization research it has been recognized that aggregation potentially has a negative influence on the fluid bed behavior with drastic consequences such as defluidization and process shutdown (Bartels et al., 2008).

The efficiency of a flocculation process depends on the strength and reach of the attractive interparticle forces that bring about aggregation. It also depends on the hydrodynamic conditions, even if the solids settle through a quiescent liquid. For aggregation to happen, particles need to have non-zero relative velocities so that collision can occur after which particles potentially stick together. If, as is the case here, the primary particles are big enough to rule out Brownian motion, relative velocities between particles are the result of different settling velocities for differently sized particles (and/or differently sized aggregates), and the randomness of the particle configuration that makes the direct environment of each particle different and thus its settling velocity.

Relative velocities amongst solids and between fluid and solid not only promote flocculation, they also provide mechanisms for breaking aggregates. Breakage can be the result of hydrodynamic stresses induced by liquid deformation around the aggregates, or the result of collisions that are energetic enough to break bonds between primary particles thereby destabilizing aggregates.

This paper focuses on the interplay between attraction and subsequent aggregation of particles and the disruption of the aggregation process as a result of hydrodynamic effects and collisions. The only driving force for solids as well as fluid motion considered here is gravity in the presence of a density difference between fluid and solid. The means of investigation is numerical simulation with full resolution of the flow and the solid particle motion. It allows us to carefully control the solid–liquid systems. The solids in the simulations are spheres all having the same size (radius a) and density (ρ_p); the spheres will be referred to as

* Address: School of Engineering, University of Aberdeen, Aberdeen, AB24 3UE, UK.

E-mail address: jderksen@abdn.ac.uk

primary particles to clearly distinguish them from aggregates. The solids occupy a fraction $\bar{\phi}$ of the total volume (the overbar denotes volume averaging), the rest is liquid. The liquid is Newtonian with uniform density (ρ) and kinematic viscosity (ν).

The spheres are attracted to one another as the result of a square-well potential (Smith et al., 1997): If the centers of two approaching spheres come within a distance $2(a + \delta)$ they trade potential energy for kinetic energy (by an amount E_{swp} per sphere). They then are within one another's square-well potential (SqWP) and are considered attached; not rigidly attached though. They keep on moving relative to one another and possibly undergo collisions. Two attached spheres can only separate if they are able to overcome the potential energy barrier imposed by the SqWP with their kinetic energy (see the subsequent section for a more detailed description). The particle interaction potential is thus defined by two parameters: the depth of the well (E_{swp}) and its width (δ). The attachment process is fully reversible.

The choice for a SqWP as the source of aggregation was instigated by its generality, numerical efficiency, and – related – simplicity (it can be effectively incorporated in the event-driven, hard-sphere algorithm that we use for particle–particle collisions). Since in this paper we do not deal with a specific aggregating system we need a generic source of aggregation that captures the two key aspects of an attractive interaction: an interaction distance and an interaction strength (δ and E_{swp} respectively).

Our flow domains are fully (in all three dimensions) periodic thereby mimicking sedimentation in large containers, away from walls. The desire to resolve the flow down to the particle scale and the related resolution requirements limits the size of the periodic domains; we do (albeit marginally) capture the $20a\bar{\phi}^{-1/3}$ correlation length scale associated with velocity fluctuations in sedimentation (Guazzelli, 2001; Snabre et al., 2009). The solids are non-deformable spheres that (next to interacting through a SqWP) undergo hard-sphere collisions in which surface roughness is parameterized with a friction coefficient. The spheres translate and rotate and their surface velocity is locally matched with the fluid velocity (no-slip). The fluid motion that is induced in this way exerts forces and torques on the spheres that (along with gravity) are used to update their linear and rotational velocities, and subsequently their position. The liquid flow is solved by means of the lattice-Boltzmann method (Chen and Doolen, 1998; Succi, 2001) with the no-slip conditions at the sphere surfaces imposed by an immersed boundary method (Goldstein et al., 1993; Ten Cate et al., 2002). The lattice-Boltzmann method uses a uniform, cubic, fixed (non-adaptive) grid. The default resolution is such that the sphere radius a corresponds to 6 grid spacings. The fixed grid implies that we have to revert to modelling if sphere surfaces get very close and the grid is not able to represent the flow in between the spheres anymore. This is done by explicitly adding lubrication forces (Nguyen and Ladd, 2002) to the equations of motion of the spheres.

The goal of this paper is to resolve the interactions between fluid flow, collisions, and attractive potential that lead to aggregation and aggregate breakage and thus to an aggregate size distribution, and to quantify the enhanced settling of the aggregating suspension. We assess what strength of attraction is required to significantly increase settling velocities and how this depends on the key dimensionless parameters of the suspension: solids volume fraction and Reynolds number(s).

In this paper, particle-resolved simulations of suspension flow are presented. Since Ladd (1994), many studies on this topic have appeared. In these studies, the lattice-Boltzmann method is a popular way of resolving the flow of interstitial fluid. Simulations of fluid flow through static assemblies of spherical particles have been used to assess the drag force and the way it depends on the topology of the assembly and on Reynolds numbers (Hill et al.,

2001; Kandhai et al., 2003; Van der Hoef et al., 2005; Beetstra et al., 2007). Fully coupled simulations with dynamic particles have been used to e.g. study turbulence modulation by solids (Ten Cate et al., 2004; Lucci et al., 2010), and fluidization and hindered settling (Ladd, 2002; Derksen and Sundaresan, 2007). Resolved simulations involving aggregates so far have focused on drag forces on static agglomerates (Ernst et al., 2013) and on hydrodynamically induced forces inside aggregates (Derksen and Eskin, 2010). In the field of colloidal systems, Stokesian Dynamics (Brady and Bossis, 1988) is an established tool to investigate the interaction between liquid flow and aggregates/aggregation (e.g. Harshe et al., 2011).

Part of the extensive experimental research on flocculation processes investigates the impact of laminar and turbulent hydrodynamics (e.g. Bouyer et al., 2004; Flesch et al., 1999). Along with an earlier simulation study of ours (Derksen, 2012), the present paper intends to capture and visualize the solid–solid and liquid–solid interactions in dynamic aggregating systems.

The organization of this paper is as follows: In the next section the flow systems are defined. Subsequently the numerical procedure is outlined. In Section 4 first we present and interpret the results for settling velocities and drag forces in *non-aggregating* suspensions in view of what is known from the literature and to have a baseline to compare aggregating suspensions with. Then qualitative observations of the effects of aggregation on the structure of the suspension and on settling rates are provided. Average drag forces and settling velocities, aggregate size distributions and average aggregate sizes in flocculating suspensions are the subject of the next sub-section. The final section summarizes the main findings.

2. Flow systems

We consider fully periodic, three-dimensional domains of length L in the x -direction, and width W in y and z -direction. Gravity points in the negative x -direction: $\mathbf{g} = -g\mathbf{e}_x$. The domains contain incompressible Newtonian liquid (density ρ , kinematic viscosity ν) and uniformly sized solid spherical particles with radius a and density $\rho_p > \rho$. In a simulation, the overall (volume averaged) solids volume fraction $\bar{\phi}$ is a constant. The symbol ϕ is used for solids volume fraction in a general sense and (in principle) ϕ is a function of location and time, $\phi(\mathbf{x}, t)$.

Each sphere experiences a net gravity force $\mathbf{F}_g = -(\rho_p - \bar{\rho})\frac{4}{3}\pi a^3 g\mathbf{e}_x$. The term $\bar{\rho}\frac{4}{3}\pi a^3 g\mathbf{e}_x$ mimics the buoyancy force with $\bar{\rho} = \bar{\phi}\rho_p + (1 - \bar{\phi})\rho$ the mixture density. Since the simulation domain is fully periodic, net gravity on the solids needs to be balanced by a body force \mathbf{f} on the liquid. The overall force balance over the simulation domain (volume V) then reads $\mathbf{f}V(1 - \bar{\phi}) = N(\rho_p - \bar{\rho})\frac{4}{3}\pi a^3 g\mathbf{e}_x$ with N the number of spheres in the domain. With $\bar{\phi} = N\frac{4}{3}\pi a^3/V$ it then follows that $\mathbf{f} = (\bar{\rho} - \rho)g\mathbf{e}_x$ (Derksen and Sundaresan, 2007).

The average hydrodynamic force acting on a sphere follows from a force balance over the liquid: $\mathbf{F}_h = \mathbf{f}\frac{4}{3}\pi a^3\left(\frac{1}{\bar{\phi}} - 1\right)\mathbf{e}_x$. This hydrodynamic force does not include an applied pressure gradient and follows the convention for the drag force as e.g. used by Van der Hoef et al. (2005) among others (Yin and Sundaresan, 2009; Beetstra et al., 2007). The hydrodynamic force is usually partitioned in several components: drag force, added mass force, history force, etc. If we assume that the solids volume fraction is uniform throughout the domain, then \mathbf{F}_h is constant and an input parameter to the simulations. The overall result of a simulation then is the volume-average superficial slip velocity between liquid and particles: $U \equiv (1 - \bar{\phi})[\langle u \rangle - \langle u_p \rangle]$ with $\langle u \rangle$ the x -velocity averaged over the fluid volume and $\langle u_p \rangle$ the x -velocity averaged over the particle volume. In what follows, results will be mostly presented in terms of U and in terms of $F \equiv \mathbf{F}_h \cdot \mathbf{e}_x / (6\pi a \nu \rho U)$ which is

the non-dimensional x -component of \mathbf{F}_h . These definitions allow us to relate to the extensive body of research that uses this representation to characterize hydrodynamic forces in (dense) suspensions (e.g. Hill et al., 2001; Wylie et al., 2003; Kandhai et al., 2003; Van der Hoef et al., 2005). We expect the dimensionless force F to be a function of $\text{Re} \equiv U_2 a / \nu$, the overall solids volume fraction $\bar{\phi}$, and the strength of the interparticle interactions that bring about aggregation.

We use another Reynolds number which is based on the steady state settling velocity of a single sphere in an unbounded fluid: $\text{Re}_\infty \equiv \frac{U_\infty 2a}{\nu}$, where U_∞ is determined by a force balance over the sole sphere falling through the liquid. In this force balance the drag force correlation due to Schiller and Naumann (1933) is used: $C_D = \frac{24}{\text{Re}_\infty} (1 + 0.15 \text{Re}_\infty^{0.687})$. In contrast to Re , Re_∞ is an input parameter to the simulations. A non-aggregating suspension of monosized spheres is fully defined by the input parameters Re_∞ , $\bar{\phi}$, ρ_p / ρ . An increase of Re_∞ (and $\bar{\phi}$ and ρ_p / ρ constant) will lead to an increase in Re .

The spheres directly interact via a square-well potential (Smith et al., 1997) that serves as the model mechanism for aggregation. If two spheres i and j approach one another and reach a center-to-center distance $2(a + \delta)$, they enter the square well and are considered ‘attached’. At that moment an amount J is added instantaneously to the relative radial approach velocity of the two spheres:

$$\tilde{\mathbf{u}}_{pi} = \mathbf{u}_{pi} + \frac{1}{2} J \mathbf{n}, \quad \tilde{\mathbf{u}}_{pj} = \mathbf{u}_{pj} - \frac{1}{2} J \mathbf{n} \quad (1)$$

with \mathbf{u}_{pi} , \mathbf{u}_{pj} sphere velocities prior to entry, and $\tilde{\mathbf{u}}_{pi}$, $\tilde{\mathbf{u}}_{pj}$ just after entry of the SqWP, and $J = \sqrt{(\Delta \mathbf{u}_{ij} \cdot \mathbf{n})^2 + (2\Delta u)^2} + \Delta \mathbf{u}_{ij} \cdot \mathbf{n}$. The unit vector \mathbf{n} points from the center of sphere i to the center of sphere j , $\Delta \mathbf{u}_{ij} \equiv \mathbf{u}_{pj} - \mathbf{u}_{pi}$, and Δu is the parameter defining the strength of the SqWP (see below). Note that for two approaching spheres $\Delta \mathbf{u}_{ij} \cdot \mathbf{n} < 0$ and thus $J = 0$ if $\Delta u = 0$ (zero momentum addition if the strength of the SqWP is zero).

In terms of interaction energy, the above implies that upon entering the square well, potential energy is converted in kinetic energy by an amount $2E_{swp} = 2(\frac{1}{2} m_p (\Delta u)^2)$ (with $m_p = \frac{4}{3} \pi \rho_p a^3$ the mass of one sphere). Since there are two spheres involved in the process, on average each sphere gains E_{swp} kinetic energy. Once in each other’s square well, the spheres keep moving under the influence of hydrodynamic forces and likely undergo one or more hard-sphere collisions according to the two-parameter model (restitution coefficient e and friction coefficient μ) of Yamamoto et al. (2001).

If two attached spheres move apart and reach the edge of the SqWP – i.e. have a center-to-center distance of $2(a + \delta)$ – they need sufficient kinetic energy to escape: they need a relative radial separation velocity $\Delta \mathbf{u}_{ij} \cdot \mathbf{n}$ (when the spheres are separating this inner product is positive) of at least $2\Delta u$. If they are able to escape, kinetic energy is converted back to potential energy upon escaping. If they are not able to escape they reverse their relative radial velocity at the moment they reach the edge of the square well and stay attached. The square-well potential is thus defined by two parameters: its width δ and its energy E_{swp} . Rather than working with the energy, we will be working with Δu in the remainder of this paper; they are related according to $E_{swp} = \frac{1}{2} m_p (\Delta u)^2$.

This leaves us with four parameters governing direct (as opposed to hydrodynamic) particle–particle interactions. In dimensionless terms these are the collision parameters e (restitution coefficient) and μ (friction coefficient), and the square-well potential parameters $\frac{\delta}{a}$ and $\frac{\Delta u}{U_\infty}$. In this study we restrict ourselves to fully elastic and smooth (frictionless) collisions so that $e = 1$ and $\mu = 0$.

3. Modeling approach

We use the lattice-Boltzmann (LB) method (Chen and Doolen, 1998; Succi, 2001) to solve for the flow of interstitial liquid. The method has a uniform, cubic grid (grid spacing Δ). The specific scheme employed here is due to Somers (1993); also see Eggels and Somers (1995). The no-slip condition at the spheres’ surfaces was dealt with by means of an immersed boundary (or forcing) method (Goldstein et al., 1993; Ten Cate et al., 2002). In this method, the sphere surface is defined as a set of closely spaced points (the typical spacing between points is 0.7Δ), not coinciding with lattice points. At these points the (interpolated) fluid velocity is forced to the local velocity of the solid surface according to a control algorithm. The local solid surface velocity has contributions from translational and rotational motion of the sphere under consideration. Adding up (discrete integration) per spherical particle of the forces needed to maintain no-slip provides us with the force the fluid exerts on the spherical particle. Similarly the hydrodynamic torque exerted on the particles can be determined. Forces and torques are subsequently used to update the linear and rotational equations of motion of each particle.

It should be noted that having a spherical particle on a cubic grid requires a calibration step, as earlier realized by Ladd (1994). He introduced the concept of a hydrodynamic radius. The calibration involves placing a sphere with a given radius a_g in a fully periodic cubic domain in creeping flow and (computationally) measuring its drag force. The hydrodynamic radius a of that sphere is the radius for which the measured drag force corresponds to the expression for the drag force on a simple cubic array of spheres due to Sangani and Acrivos (1982) which is an extension towards higher solids volume fractions of the analytical expression due to Hasimoto (1959). Usually a is slightly larger than a_g with $a - a_g$ typically equal to half a lattice spacing or less. Most of the simulations presented in this paper have a resolution such that $a = 6\Delta$. In some cases to be discussed below we assessed the effect of resolution by comparing the same physical situations on grids with different resolutions ($a = 6\Delta$, $a = 8\Delta$, $a = 12\Delta$).

Once the spatial resolution is fixed, the temporal resolution of the LB simulations is determined by the choice of the kinematic viscosity ν . The kinematic viscosity varied between 0.02 and 0.005 in lattice units (space unit is Δ , time unit is one time step Δt) so that for the default resolution ($a = 6\Delta$) the viscous time scale a^2/ν corresponds to 1800 to 7200 Δt . The convective time scale a/U_∞ is in the range of 200–600 Δt .

The viscosity is determined by the desired value for $\text{Re}_\infty \equiv U_\infty 2a/\nu$ and by the constraint to keep fluid velocities well below the speed of sound $c_s = \sqrt{2}/2$ (in lattice units) of the (compressible) lattice-Boltzmann scheme to achieve approximately incompressible flow; if $U_\infty = O(0.01c_s)$ the flow is practically incompressible. Once a , ν and U_∞ have been set, the value for gravitational acceleration g is determined so as to actually achieve U_∞ : $g = \frac{3}{8} C_D \frac{\rho}{\rho_p - \rho} \frac{U_\infty^2}{a}$ with $C_D(\text{Re}_\infty)$ based on the Schiller–Naumann correlation.

The fixed-grid simulations involving moderately dense suspensions as discussed here require explicit inclusion of sub-grid lubrication forces (Nguyen and Ladd, 2002). For creeping flow, the expression for the radial lubrication force on two equally sized solid spheres i and j having relative velocity $\Delta \mathbf{u}_{ij} \equiv \mathbf{u}_{pj} - \mathbf{u}_{pi}$ reads (Kim and Karrila, 1991)

$$\mathbf{F}_{lub} = \frac{3}{2} \pi \rho \nu a^2 \frac{1}{s} (\mathbf{n} \cdot \Delta \mathbf{u}_{ij}), \quad \mathbf{F}_{lub,j} = -\mathbf{F}_{lub,i}, \quad \mathbf{F}_{lub,i} = F_{lub} \mathbf{n} \quad (2)$$

with s the smallest distance between the sphere surfaces $s \equiv |\mathbf{x}_{pj} - \mathbf{x}_{pi}| - 2a$, and (again, see above) \mathbf{n} the unit vector pointing from the center of sphere i to the center of sphere j . Since Eq. (2) is

based on a creeping flow assumption in the narrow gap between closely spaced spheres undergoing relative motion it is valid if $Re_s \equiv \frac{s|\Delta\mathbf{u}_{ij}|}{\nu} \ll 1$. Tangential lubrication forces and torques have not been considered since they are much weaker than the radial lubrication force; the former scale with $\ln(\frac{a}{s})$, the latter (see Eq. (2)) with $\frac{a}{s}$. The expression in Eq. (2) has been tailored for use in lattice-Boltzmann simulations according to Nguyen and Ladd (2002): (1) The lubrication force needs to be switched off when sphere surfaces are sufficiently far apart in which case the grid associated with the LBM can accurately account for the hydrodynamic interaction between the spheres (typically if $s > \Delta$). (2) The lubrication force needs to saturate when solid surfaces are very close to account for surface roughness and to avoid very high levels of the lubrication force that could lead to unphysical instabilities in the simulations. To achieve Objective (1) instead of Eq. (2) one writes

$$F_{lub} = \frac{3}{2}\pi\rho\nu a^2 \left(\frac{1}{s} - \frac{1}{s_0}\right) (\mathbf{n} \cdot \Delta\mathbf{u}_{ij}) \text{ if } s \leq s_0, \text{ and } F_{lub} = 0 \text{ if } s > s_0 \quad (3)$$

with the modelling parameter s_0 as the distance between solid surfaces below which the lubrication force becomes active. For Objective (2) a second modelling parameter s_1 is introduced as the distance below which the lubrication force saturates: $F_{lub} = \frac{3}{2}\pi\rho\nu a^2 \left(\frac{1}{s_1} - \frac{1}{s_0}\right) (\mathbf{n} \cdot \Delta\mathbf{u}_{ij})$ if $s \leq s_1$. The settings for s_0 and s_1 were $s_0 = 0.2a$ and $s_1 = 2 \times 10^{-4}a$. With this procedure and these settings accurate results for close-range hydrodynamic sphere-sphere interactions have been reported (Nguyen and Ladd, 2002; Derksen and Sundaresan, 2007).

The spheres' equations of linear and rotational motion including resolved and unresolved (i.e. lubrication) forces are integrated according to an Euler forward scheme. These time-step driven updates are linked with an event-driven algorithm that detects events related to the SqWP and to hard-sphere collisions during the Euler time steps. Three types of events can be distinguished: (1) a hard-sphere collision; (2) two approaching spheres enter one another's SqWP; (3) two spheres that move apart reach a center-to-center distance of $2(a + \delta)$ and attempt to leave one another's SqWP. Event (3) has two possible outcomes: the spheres detach (if their separating relative velocity is sufficiently high), or do not detach. Once an event is being detected, all particles are frozen and the event is carried out which for all three event types implies an update of the linear velocities (and also angular velocities for event type (1) if $\mu \neq 0$) of the two spheres involved in the event. Subsequently all spheres continue moving until the end of the time step, or until the next event, whichever comes first.

The initial condition is a domain that contains solid and liquid at rest and the (non-overlapping) spheres randomly distributed in the domain. Then gravity is switched on while $\Delta u = 0$ (inactive SqWP) and the system is evolved to a dynamically stationary state. Once this state has been reached (typically after $t = O(100a/U_\infty)$), the strength of the SqWP Δu is set to its desired value and we let the solid-liquid system adapt itself to this new condition.

Table 1
Dimensionless input parameters defining the simulation cases and their settings.

Parameter	Description	Status	Value or range
$\bar{\phi}$	Solids volume fraction	Varied	0.12–0.32
Re_∞	Single particle settling Reynolds number	Varied	6–72
ρ_p/ρ	Density ratio	Fixed	4.0
$\Delta u/U_\infty$	SqWP escape velocity over settling velocity	Varied	0.005–0.030
δ/a	SqWP width over sphere radius a	Fixed	0.025
e	Restitution coefficient	Fixed	1.0
μ	Friction coefficient	Fixed	0.0
L/a	Domain length over a	Default	48
L/W	Domain length over domain width	Fixed	2
s_0/a	Onset distance of lubrication force over a	Fixed	0.2
s_1/a	Saturation distance of lubrication force over a	Fixed	2×10^{-4}

3.1. Dimensionless parameters

Table 1 summarizes the non-dimensional input parameters defining the simulations. It also shows which parameters have been set to *fixed* values, which parameters have a *default* value the effect of which has been investigated for a few cases, and which parameters have been *varied* independently (the table then shows the range of variation). As can be seen, we cover part of a three-dimensional parameter space with independently varied coordinates $\bar{\phi}$, Re_∞ , and $\Delta u/U_\infty$. Note that a Stokes number can be defined by combining Re and the (in this study constant) density ratio $\frac{\rho_p}{\rho}$ to $St = \frac{2}{9} \frac{\rho_p}{\rho} Re$.

The number of primary spheres in a simulation varies between 790 ($\bar{\phi} = 0.12$) to 2112 ($\bar{\phi} = 0.32$) for the default domain size simulations. The largest number of spheres in a single simulation is 18,796 for a simulation with domain size $L/a = 108$ and $\bar{\phi} = 0.25$. Simulations on default domain sizes run in sequential mode on (2011) standard PC hardware. Runtimes per simulation are 2–4 weeks (total, i.e. start-up and steady state for collecting statistical information).

4. Results

4.1. Drag in non-aggregating systems

To have a baseline to compare drag in aggregating suspensions with, first drag in non-aggregating suspensions is considered. Results for non-aggregating systems also allow for comparisons with results reported in the literature. In Fig. 1a our data of the average, non-dimensional drag force as a function of $Re \equiv U_2 a/\nu$ have been summarized. Averaging is done over the entire flow domain and over time after a dynamic stationary state has been reached. In the remainder of Fig. 1 we present further data and data analysis of drag in suspensions of mono-sized, non-aggregating particles.

The curves in Fig. 1 that represent the correlation due to Beetstra et al. (2007) have been added for reference. In their paper they summarized their computational (lattice-Boltzmann) results for drag on random assemblies of *static* spheres at intermediate Reynolds numbers with the following correlation:

$$F(\phi, Re) = \frac{0.413}{24(1-\phi)^2} \left[\frac{(1-\phi)^{-1} + 3\phi(1-\phi) + 8.4Re^{-0.343}}{1 + 10^{3\phi} Re^{-(1+4\phi)/2}} \right] \quad (4)$$

(Re up to 1000, ϕ up to 0.6). In the Reynolds number and solids volume fraction range we are interested (see Table 1), Beetstra et al report that the deviation between the correlation (Eq. (4)) and their actual simulation results is typically 10%. Our drag data shown in Fig. 1a generally differ by a larger amount from the correlation.

We demonstrate that the difference is there for physical, not for numerical reasons. For this we first present drag data for static assemblies. With the same numerical approach, spatial resolution,

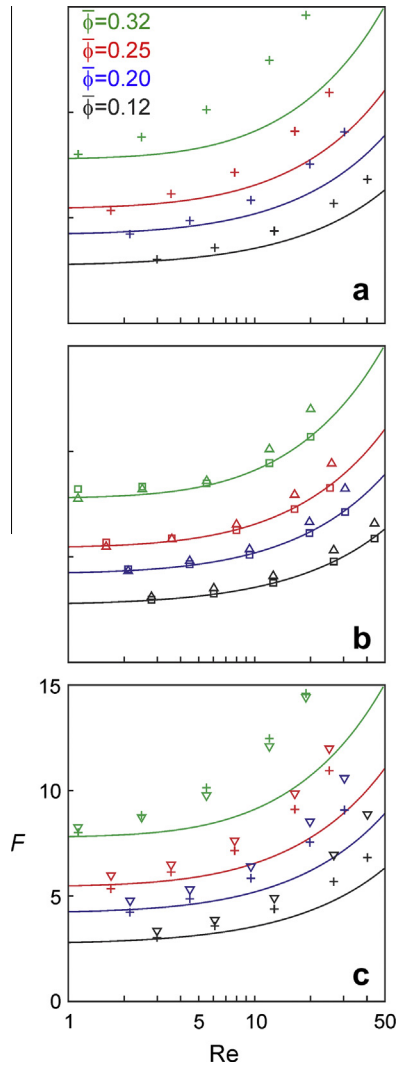


Fig. 1. Dimensionless drag force as a function of Re for four different overall solids volume fractions $\bar{\phi}$. The drawn curves in each panel represent the correlation due to Beetstra et al (Eq. (4)). Panel (a) *plusses* (+) dynamic simulations; panel (b) *squares* (□): static random sphere assemblies and *triangles* (Δ): static sphere assemblies frozen from dynamic simulations; panel (c) *inverted triangles* (∇): Eq. (5) and *plusses* (+) dynamic simulations (same data as in (a)).

and domain size as used for the dynamic simulations, simulations of the flow through purely random assemblies of *fixed* spheres were performed. In terms of the average drag on a sphere these simulations are in good agreement with Eq. (4), see the square symbols in Fig. 1b. The way the spheres are arranged has some impact on the drag for static assemblies: In Fig. 1b we also show results for the drag force from simulations with spheres in fixed locations with the locations now taken from snapshots of the dynamic simulations. The drag force in the static assemblies increases as a result of this change in topology, with the level of increase a distinct function of the Reynolds number: virtually no increase at low Re , and a significant effect for Re beyond 10.

The topologies of the sphere assemblies (random versus snapshots from settling spheres) have been analysed at the micro-level in terms of radial and angular distribution functions (in Fig. 2), and at the macro-level by identifying the presence of larger inhomogeneities, such as traveling voidage waves (in Fig. 3). As has been demonstrated by Duru et al. (2002) and Derksen and Sundaresan (2007), the latter can be identified by making space-time plots of the solids volume fraction as we do in Fig. 3.

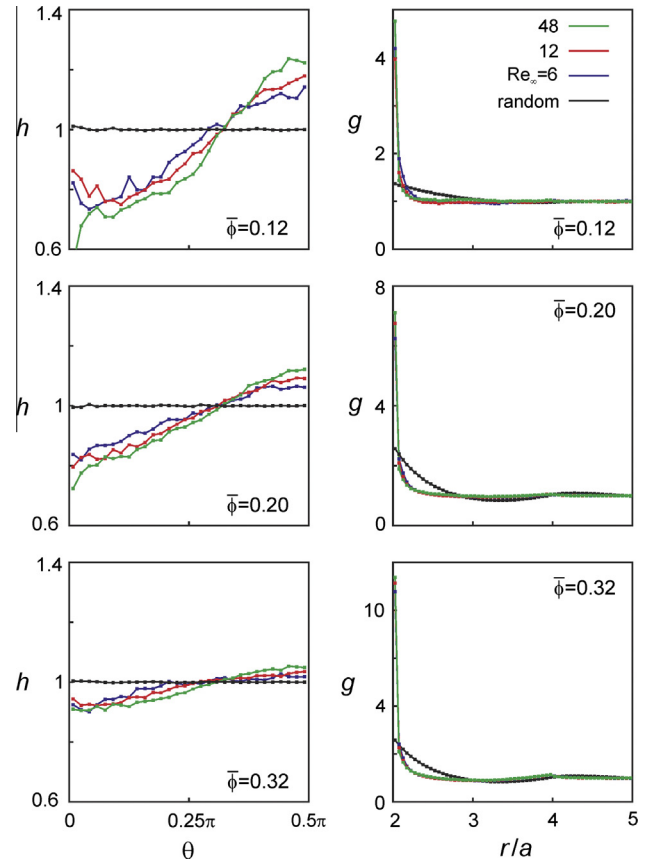


Fig. 2. Left: angular distribution functions $h(\theta)$; right: radial distribution functions $g(r)$ for random sphere assemblies and for dynamic assemblies at various Reynolds numbers and at various solids volume fractions $\bar{\phi}$. The resolution in θ is $\frac{\pi}{60}$, in r it is $0.05a$. The angular distribution function only considers sphere pairs that have a center-to-center distance less than $3a$. $\theta = 0$ corresponds to a vertical orientation.

For characterizing the microstructure of the suspensions, radial and angular distribution functions have been determined. The radial distribution function $g(r)$ is defined such that $g(r)dr$ is the probability of having a sphere center located in a spherical shell with radius r and thickness dr around a (reference) sphere. This probability is normalized by the probability for a homogeneous distribution of sphere centers. In a similar manner $h(\theta)d\theta$ (with $h(\theta)$ the angular distribution function) is the normalized probability of finding a sphere relative to a reference sphere in a conical shell with top angle between θ and $\theta + d\theta$. The angle θ has been defined such that $\theta = 0$ is in the x -direction which is the direction of gravity. When determining $g(r)$ and $h(\theta)$ from actual sphere configurations, instead of dr and $d\theta$ we use a finite size $\Delta r = 0.05a$ and $\Delta\theta = \frac{\pi}{60}$ respectively, and we average over at least 250 statistically independent configurations each consisting of 790 spheres (if $\bar{\phi} = 0.12$) to 2112 spheres ($\bar{\phi} = 0.32$). For the angular distribution function the search for sphere centers is limited to a distance $r = 3a$ from the reference sphere center. Given the steep slope of $g(r)$ for $r \downarrow 2a$ in the dynamic simulations, it should be noted that the estimate of $g(2a + \frac{1}{2}\Delta r)$ significantly depends on the choice of Δr . Throughout the paper $\Delta r = 0.05a$ has been used so that at least we can mutually compare radial distribution functions.

The microstructure of the settling suspension is clearly different from a purely random microstructure (see Fig. 2). The purely random structure does not show angular preference and the radial distribution function is what is to be expected from a hard-spheres gas (e.g. Verlet and Weis, 1972; Yin and Sundaresan, 2009). The settling suspension has a much higher probability for closely

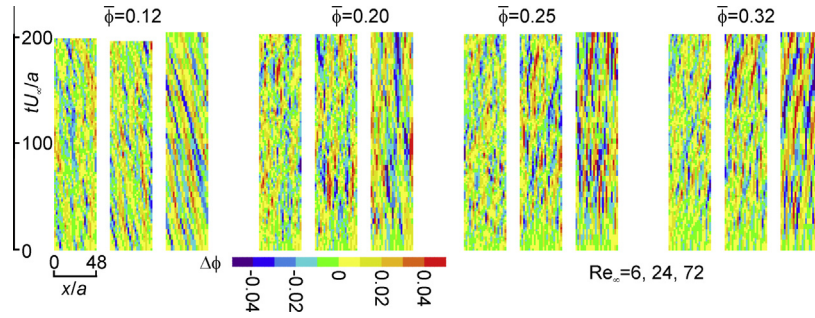


Fig. 3. Space-time plots of the solids volume fraction in various simulations. For each of the four average solids volume fractions, three Reynolds numbers are considered: $Re_\infty = 6, 24,$ and 72 (from left to right). $\Delta\phi$ indicates the deviation from the volume-average $\bar{\phi}$.

spaced spheres (much higher $g(r \downarrow 2a)$ compared to random assemblies). There also is a preference for spheres to settle side-by-side: $h(\theta = \pi/2) > 1$, specifically for the lower solids volume fractions. These preferential positions and also orientations are, however, largely independent of the Reynolds number. It therefore seems unlikely that they are responsible for the Reynolds-dependent increase in drag as witnessed in Fig. 1b.

The presence and strength of larger scale inhomogeneities (see the space-time plots in Fig. 3) does depend on Re , with more pronounced spatial and temporal solids volume fraction variations for larger Re . Such spatial variation in ϕ do enhance overall average drag in suspensions of static spheres given the stronger-than-linear relation between ϕ and the drag force; the relatively dense regions contribute more strongly to a drag increase than the dilute regions contribute to a drag decrease.

The increase in drag as a result of the changing topology is clearly not enough to fully explain the differences between dynamic, settling suspensions, and static, purely random sphere assemblies (as previously observed in Fig. 1a). Next to a different topology, also the spheres' dynamics is expected to increase the drag force. Saffman (1973) highlighted fundamental differences between dilute suspensions of freely moving particles and particles held rigidly under creeping flow conditions. At higher Reynolds numbers and for denser systems, Wylie et al. (2003) showed that erratic motion of solid particles in addition to an average relative velocity between the solids and the fluid enhances drag. They proposed a correlation that considers this effect:

$$F(\phi, Re, Re_T) = F(\phi, Re, 0) + Re \left[0.0336 + 0.106\phi + \frac{0.0116}{(1-\phi)^5} \right] \times \left[\left(1 + \frac{2Re_T^2}{Re^2} - \frac{Re_T^4}{Re^4} \right) \operatorname{erf} \left(\frac{Re}{\sqrt{2}Re_T} \right) + \sqrt{\frac{2}{\pi}} \frac{Re_T}{Re} \left(1 + \frac{Re_T^2}{Re^2} \right) \exp \left(-\frac{Re^2}{2Re_T^2} \right) \right] \quad (5)$$

Dimensionless drag F is now also a function of $Re_T \equiv T^{1/2}2a/\nu$ with T the granular temperature. For the term $F(\phi, Re, 0)$ in Eq. (5) we use the expression in Eq. (4). In order to analyse our results in light of Eq. (5), first the granular temperature has been extracted from our dynamic simulations, see Fig. 4. Substituting the Re_T data in Eq. (5), along with the Reynolds numbers associated to the average velocity provides us with drag force result that are represented by the inverted triangles in Fig. 1c. For $\bar{\phi} = 0.32$ this granular temperature effect very well represents the increased drag in the dynamic simulations. For the lower solids volume fractions Eq. (5) systematically overpredicts the dynamic drag. An overprediction – to a lesser extent though – was also observed by Wylie et al. (2003) when they compared their equation (Eq. (5)) with accompanying lattice-Boltzmann simulations. We speculate that

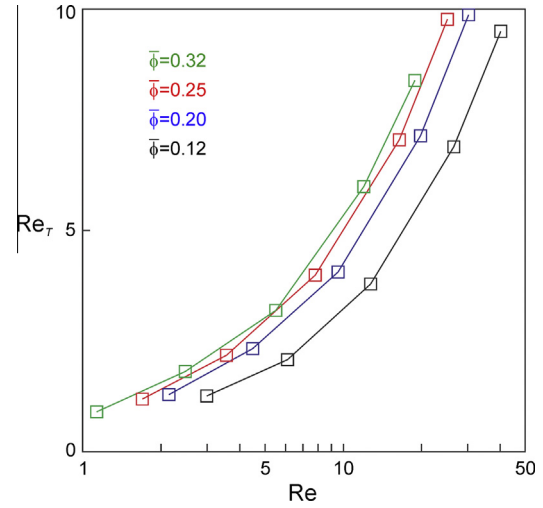


Fig. 4. Reynolds number based on the granular temperature (Re_T) as a function of Re for various $\bar{\phi}$. The symbols are connected by straight lines to guide the eye only.

part of the deviations are also due to the fluctuating motion in our dynamic simulations being correlated to the local hydrodynamic (liquid and solid) environment of particles, i.e. the solids fluctuations are less random compared to the purely random ones Wylie et al used in their work.

We conclude that our results for the drag in dynamic, non-aggregating, settling suspensions show similar features and dependencies as observed in previous works: (1) there is agreement with earlier work on drag in random, static sphere assemblies; (2) drag clearly increases with an increase in solids volume fraction ('hindered settling') and with increasing Reynolds number; (3) the spheres do not arrange themselves purely randomly which adds to the average drag force; (4) the fluctuating motion of the spheres increase the drag force (in qualitative agreement with Wylie et al., 2003).

4.2. Verifications: system size and resolution

A number of simulations were run to assess the effect of the domain size and the spatial resolution (the latter quantified by the number of lattice spacings spanning one sphere radius a) on F . The linear domain size L has been varied between $32a$ and $108a$, while keeping the aspect ratio L/W constant (at 2). For cases with the same $\bar{\phi}$ and Re_∞ the dimensionless drag F and Re based on superficial slip velocity differ by 4% at most between domain sizes. These differences are small compared to effects discussed in the previous section that e.g. related to drag on moving versus drag on static spheres. A total of four domain sizes were probed for

$\bar{\phi} = 0.20$. The fluctuations length scale $20a\bar{\phi}^{-1/3}$ (Guazzelli and Hinch, 2011) then is equal to $34a$ which is inside the range of widths W covered by the four domains (W from $16a$ to $54a$). The consequences of capturing/not capturing the fluctuations length scale for the average drag force are seemingly marginal.

Relative differences are also small when resolution is changed. The default resolution is $a = 6$. Refinements of $a = 8$ and 12 have been investigated. With all other dimensionless settings constant, the largest deviation in terms of F amounts to 1.5% .

4.3. Impressions of aggregating systems

We begin the discussion on aggregating systems by presenting qualitative results. As a metric for the level of aggregation, the average number of sphere–sphere contacts per sphere (C_{sph}), i.e. the number of spheres that are within a center-to-center distance of $2(a + \delta)$ of a certain test sphere, is considered. In Fig. 5 we show time series of C_{sph} . At moment $t = 0$, when the non-aggregating suspension is in a stationary state, the square-well potential is switched on, i.e. we switch from $\Delta u = 0$ to the values as indicated in the figure. The result is an increase in C_{sph} to an extent that clearly depends on the strength of the potential. With respect to solids volume fraction $\bar{\phi}$ and single-sphere-settling Reynolds number Re_∞ , the level of aggregation follows to-be-expected trends: denser systems aggregate more, whereas the more vigorous motion and higher (liquid and solids) inertia and associated collisions for the higher Reynolds numbers limit aggregation levels. Impressions of sphere configurations are given in Fig. 6. From this figure the size of the simulation domains and the aggregate structures being formed can be gauged.

For $\bar{\phi} = 0.32$ (the lower panels in Fig. 5) and $\frac{\Delta u}{U_\infty} \geq 0.020$ aggregation gets so strong that eventually one very large aggregate forms that contains almost all primary spheres and has a size of the order of the domain size. In some of these cases (see Fig. 5) a steady state is not reached within a time window of $200a/U_\infty$. Given the fully periodic boundary conditions, the single, large aggregate interacts with itself and the settling velocity and drag force results are not representative for large, homogeneous systems anymore. For this reason, aggregating systems with $\bar{\phi} = 0.32$ will not be discussed further.

The square-well potential and consequential aggregation clearly enhances the settling rates, see Fig. 7. The remarkable feature of the results in this figure is that the settling speed enhancement is a strong function of Re_∞ . For the higher Re_∞ (and thus higher Stokes numbers; note that the density ratio is constant in this work) inertia promotes collisions and liquid deformation which are two effects that break aggregates and thus keeps the spheres less attached. The result is a more spatially uniform distribution of primary particles and only a minor increase of their settling rates.

We need to revisit the sensitivity of the domain size, now for aggregating systems, as aggregates get significantly larger than the primary spheres and potential self-interaction of large aggregates through the periodic boundaries is a concern. We have probed the domain size sensitivity by monitoring the transition from a non-aggregating to an aggregating suspension for two physical cases with $(\bar{\phi}, Re_\infty, \Delta u/U_\infty) = (0.20, 48, 0.03)$ and $(0.25, 12, 0.02)$ respectively. These are cases with relatively strong interaction and (the latter case) relatively high $\bar{\phi}$, so that aggregation is significant. For these two physical cases results on two domains (with $L = 48a$ and with $L = 72a$) have been compared in Fig. 8. There

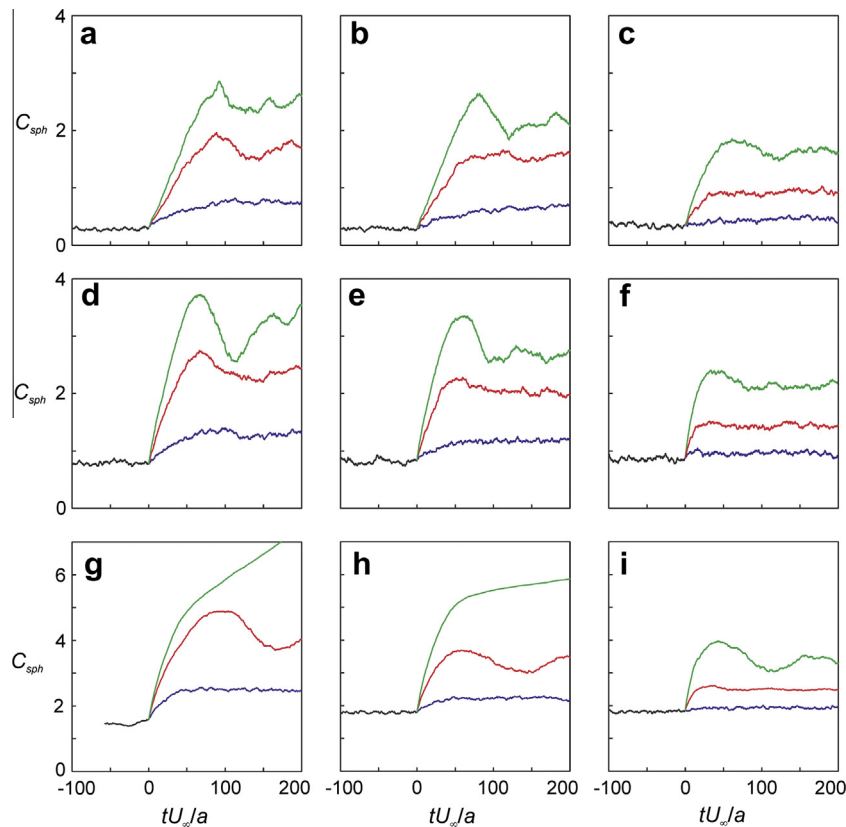


Fig. 5. Time series of the number of contact points per sphere C_{sph} . Top row: $\bar{\phi} = 0.12$; middle row: $\bar{\phi} = 0.20$; bottom row: $\bar{\phi} = 0.32$. Left column: $Re_\infty = 6$; center column: $Re_\infty = 12$; right column: $Re_\infty = 48$. Black: $\Delta u/U_\infty = 0$; blue: $\Delta u/U_\infty = 0.01$; red: $\Delta u/U_\infty = 0.02$; green: $\Delta u/U_\infty = 0.03$. At $t = 0$ Δu switches from zero to the indicated non-zero values. (For interpretation of the references to colour in this figure legend, the reader is referred to the web version of this article.)

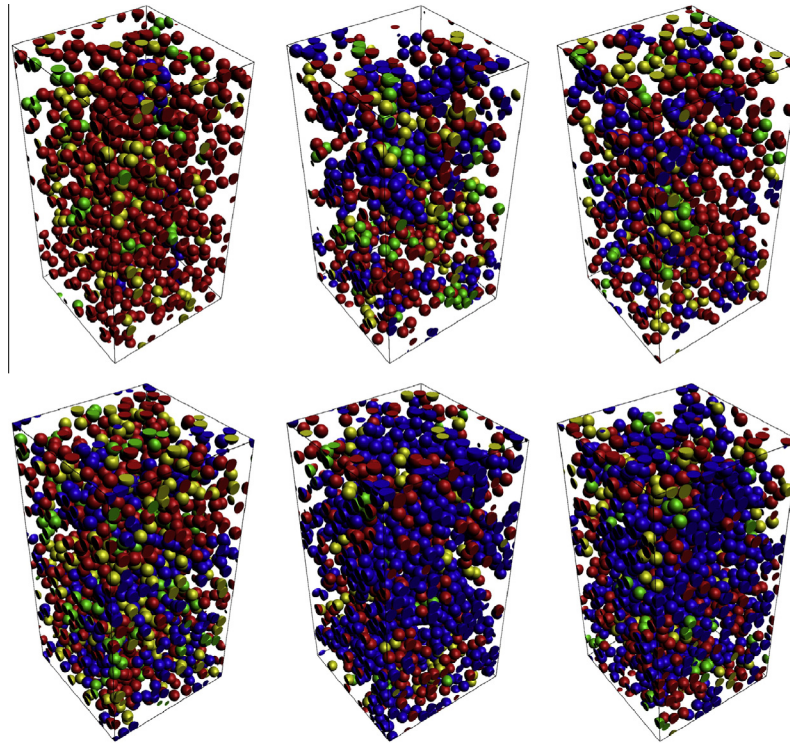


Fig. 6. Single realizations of sphere positions under stationary conditions with spheres colored according to the aggregate they are part of. Top row $\bar{\phi} = 0.12$; bottom row $\bar{\phi} = 0.20$. Left $Re_\infty = 6$ and $\Delta u/U_\infty = 0$; middle: $Re_\infty = 6$ and $\Delta u/U_\infty = 0.03$; right $Re_\infty = 48$ and $\Delta u/U_\infty = 0.03$. Red are single spheres, green spheres are part of doublets, yellow spheres are part of triplets, and blue spheres are in aggregates of four or more primary spheres. (For interpretation of the references to colour in this figure legend, the reader is referred to the web version of this article.)

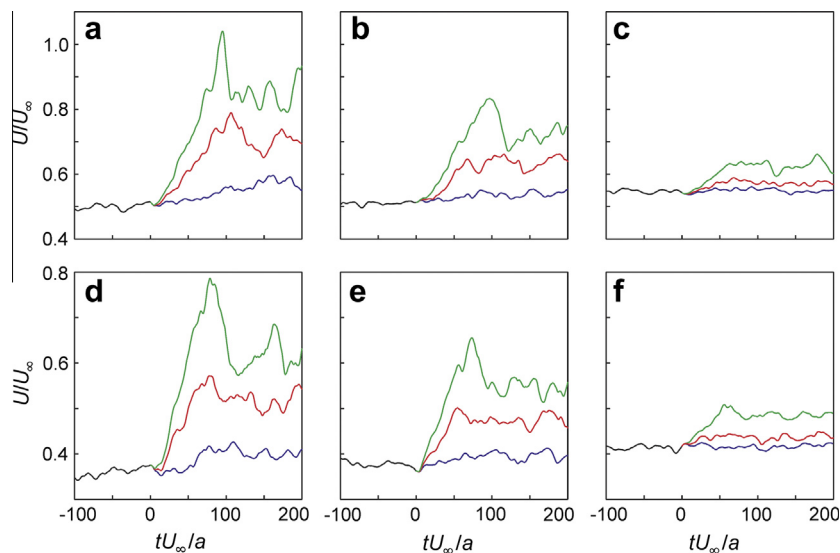


Fig. 7. Time series of sphere-averaged slip velocity U normalized with U_∞ . Top row: $\bar{\phi} = 0.12$; bottom row: $\bar{\phi} = 0.20$. Left column: $Re_\infty = 6$; center column: $Re_\infty = 12$; right column: $Re_\infty = 48$. Black: $\Delta u/U_\infty = 0$; blue: $\Delta u/U_\infty = 0.01$; red: $\Delta u/U_\infty = 0.02$; green: $\Delta u/U_\infty = 0.03$. (For interpretation of the references to colour in this figure legend, the reader is referred to the web version of this article.)

is clear agreement between standard-size and large-size domains in terms of the levels of aggregation as measured by the number of contacts per sphere, and in terms of the time needed for the systems to transit from a steady non-aggregating state to a steady aggregating state. The same holds true for the settling velocities. The generally smoother curves for the larger domains are due to the larger number of spheres over which averaging takes place.

4.4. Drag force in aggregating systems

Aggregate size distributions (ASD's) were determined based on a large number of realizations of the aggregating solid–liquid systems after they reached a dynamic steady state. Examples of mass-weighted ASD's are presented in Fig. 9. In this figure, $p(n_a)$ is the fraction of the total solids mass in the system contained in

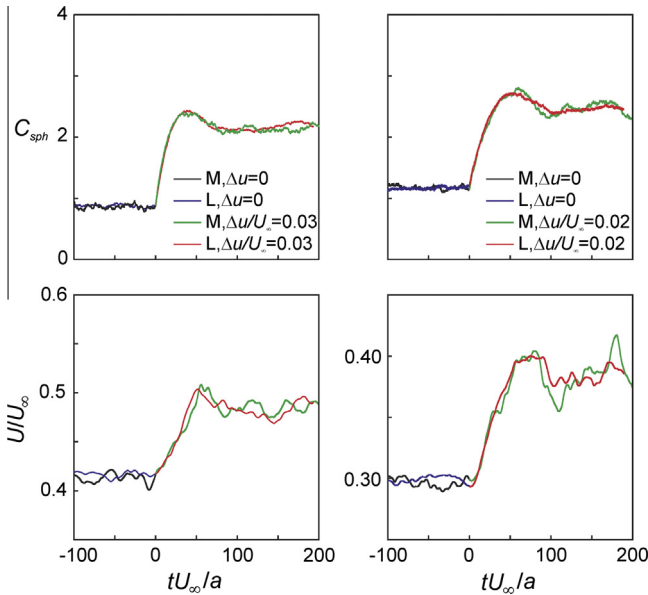


Fig. 8. Time series of the average number of contact points per sphere C_{sph} (top) and the average settling velocity U/U_∞ (bottom); comparison between the default domain (M, $L/a = 48$) and large domain (L). The latter has length $L/a = 72$. In the left two panels: $\bar{\phi} = 0.20$, $Re_\infty = 48$; in the right panels: $\bar{\phi} = 0.25$, $Re_\infty = 12$. At $t = 0$ Δu switches from zero to the indicated non-zero values.

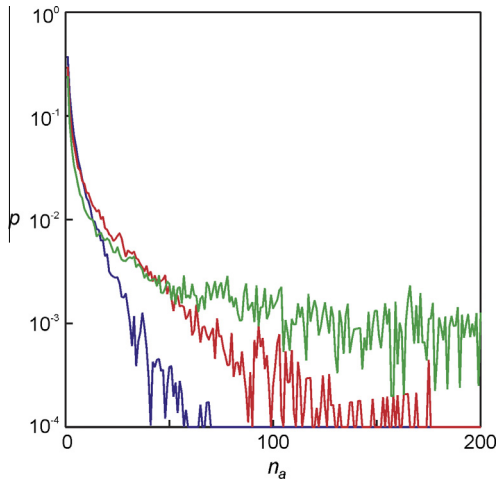


Fig. 9. Aggregate size distributions for $\bar{\phi} = 0.20$ and $Re_\infty = 12$. Blue: $\Delta u/U_\infty = 0.01$; red: $\Delta u/U_\infty = 0.02$; green: $\Delta u/U_\infty = 0.03$. The mass-weighted averages are $\langle n_a \rangle = 4.88$, 11.9, and 59.4 respectively. The total number of particles in each case is 1320. The ASD's are based on 600 realizations (with a mutual time spacing $4a/U_\infty$) after steady state was reached. p -values below 10^{-4} have been set to 10^{-4} (for plotting purposes only). (For interpretation of the references to colour in this figure legend, the reader is referred to the web version of this article.)

aggregates consisting of n_a primary spheres. Fig. 9 shows that a stronger interaction potential shifts the ASD's to the right, i.e. to (on average) larger aggregates. Given the definition of $p(n_a)$, the mass-averaged aggregate size is $\langle n_a \rangle \equiv \sum_{n_a=1}^N n_a p(n_a)$ with N the number of primary spheres in the entire flow system (at the same time N is the absolute upper limit of n_a). In Fig. 10 mass averaged aggregate size as a function of the three independent input variables $\bar{\phi}$, Re_∞ , and $\frac{\Delta u}{U_\infty}$ is presented.

There is a clear positive correlation between aggregate size and interaction potential strength. Aggregate sizes also increase with solids volume fraction. A third observation is that higher Re_∞ drastically brings down the average aggregate size. The reason

for the latter is that inertia promotes the number and intensity of particle–particle collisions as well as deformation in the liquid phase. This tends to destabilize and break aggregates, thereby shifting the size distribution towards smaller aggregates. It should be noted that the results for $\bar{\phi} = 0.25$ and $\frac{\Delta u}{U_\infty} \geq 0.025$ likely are affected by the finite domain size and finite number of primary spheres per simulation, given that the mass-averaged aggregate size (order a few hundred) are a significant fraction of the total number of spheres (1645) in these simulations. Only a few large aggregates can coexist at any moment in time.

In Fig. 11 the consequences of aggregation for the drag force are summarized. We show the average drag on a primary sphere under different aggregation conditions. The drag per primary sphere reduces most for the lower Re_∞ cases which (see Fig. 10) aggregate most. There is, however, not a one-on-one relation between aggregate size and drag reduction. This is based on the following two observations: (1) Although the amount of drag reduction for simulations with $\bar{\phi} = 0.12$ and $\bar{\phi} = 0.25$ are comparable, the aggregates in the latter cases are more than one order of magnitude larger than in the former. (2) Aggregates with significant sizes are formed for the higher Reynolds numbers, while drag is only marginally reduced. In what follows we further analyse and correlate the drag and aggregate size data in an attempt to better understand the interplay between aggregation and per-sphere reduction of drag.

The relation between drag reduction and aggregate size is examined in Fig. 12 (this figure combines the data presented in Figs. 10 and 11). In Fig. 12 the average aggregate size has been normalized with the average aggregate size for $\Delta u = 0$ (symbol $\langle n_a \rangle_{\Delta u=0}$; in non-aggregating systems there is (on average) a number of sphere centers within a range $2(a + \delta)$ of other sphere centers and those spheres are counted as attached). In all cases drag decays monotonically as a function average aggregate size, with the levels of decay dependent on $\bar{\phi}$ and Re_∞ . At comparable average aggregate size and overall solids volume fraction, the ratio $\frac{F}{F_{\Delta u=0}}$ is larger (i.e. drag decreases less) for larger Re_∞ . To study if this effect relates to the way the solids organize themselves, cases having the same $\bar{\phi}$ and approximately the same ratio $\frac{\langle n_a \rangle}{\langle n_a \rangle_{\Delta u=0}}$ but clearly different $\frac{F}{F_{\Delta u=0}}$ have been compared. For $\bar{\phi} = 0.12$ these cases are $(Re_\infty, \frac{\Delta u}{U_\infty}) = (72, 0.03)$; $(24, 0.025)$; $(12, 0.02)$; $(6, 0.05)$. These four cases all have $\frac{\langle n_a \rangle}{\langle n_a \rangle_{\Delta u=0}} \approx 2.3$ (see Fig. 12, upper-left panel). For $\bar{\phi} = 0.20$ the cases are $(Re_\infty, \frac{\Delta u}{U_\infty}) = (48, 0.03)$; $(12, 0.025)$; $(6, 0.02)$; for these three systems $\frac{\langle n_a \rangle}{\langle n_a \rangle_{\Delta u=0}} \approx 7.6$ (see Fig. 12, lower-left panel).

In Fig. 13 we show how the global structure of the suspension changes as a result of the interaction potential. Aggregation has consequences for the existence of larger-scale inhomogeneities. At zero interaction potential, larger Reynolds number cases are already inhomogeneous and the addition of the potential has only weak impact on the levels of inhomogeneity (see Fig. 13); smaller Reynolds number cases turn inhomogeneous when the interaction potential is switched on.

5. Summary and conclusions

Simulations of aggregating solids settling through liquid were presented with the aim to quantify the reduction of the average drag force per primary particle as a result of the aggregation process. The simulations explicitly resolved the no-slip conditions at solid particle surfaces, the flow of interstitial liquid and the solid-particle dynamics, including hard-sphere collisions. The tendency to aggregate was derived from an attractive square-well interaction potential. Minimal modeling was required: a radial lubrication force was added to the particles' equations of motion to compensate for the lack of resolution when particle surfaces

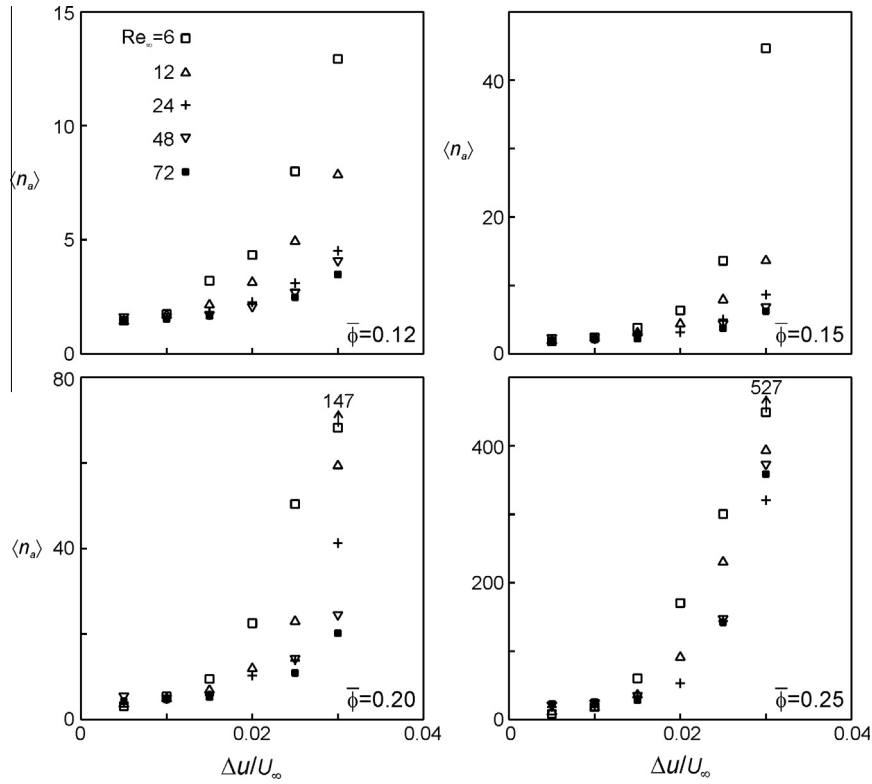


Fig. 10. Mass-average aggregate size (n_a) as a function of suspension properties.

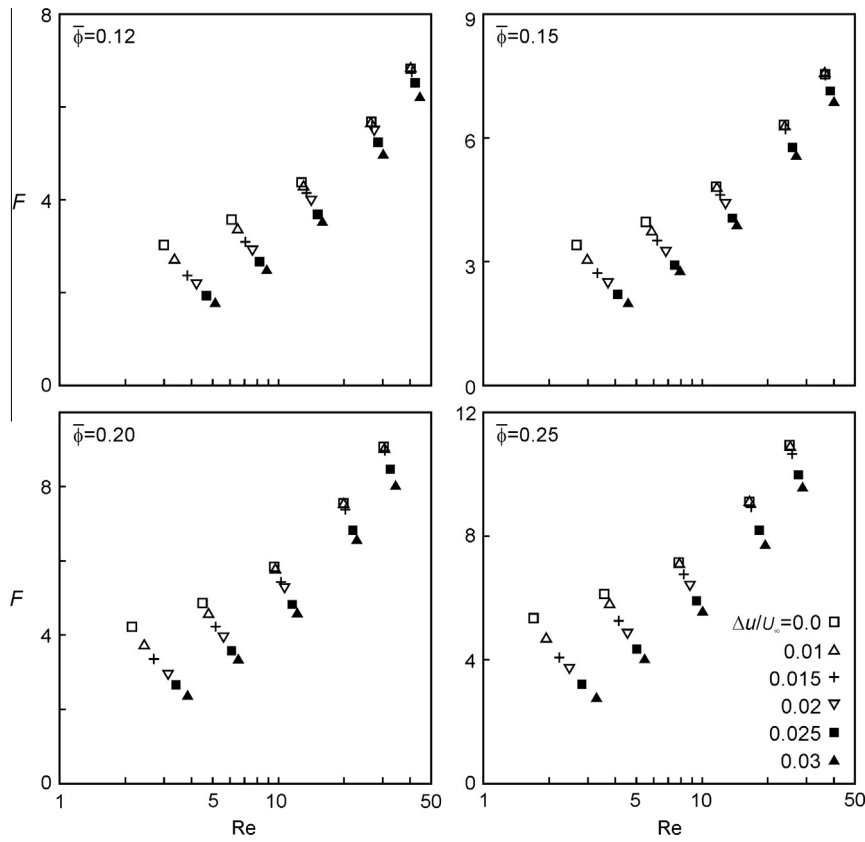


Fig. 11. Dimensionless drag force per primary sphere (F) as a function of Re for four different solids volume fractions $\bar{\phi}$ and SqWP strength Δu . The data points for $\Delta u = 0$ are the same as the ones given in Fig. 1a and c.

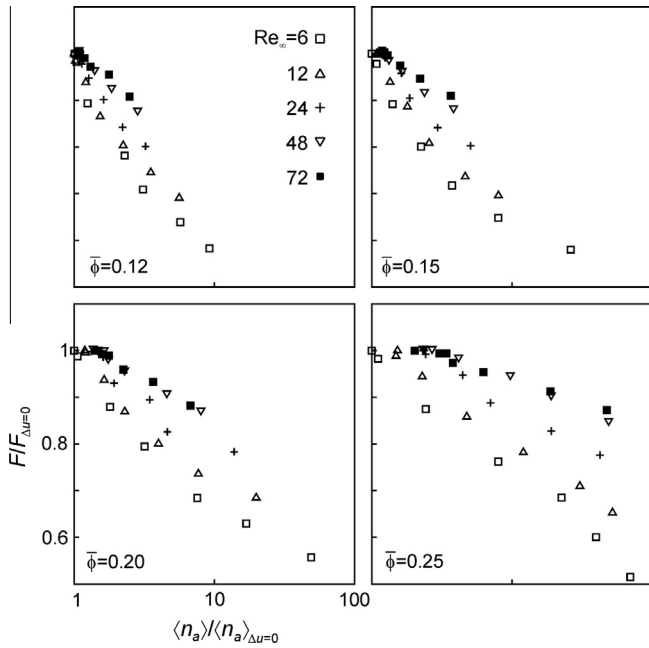


Fig. 12. Drag in aggregating systems relative to drag in non-aggregating systems $\frac{F}{F_{\Delta u=0}}$ as a function of normalized average aggregate size for solids volume fractions and Re_∞ as indicated.

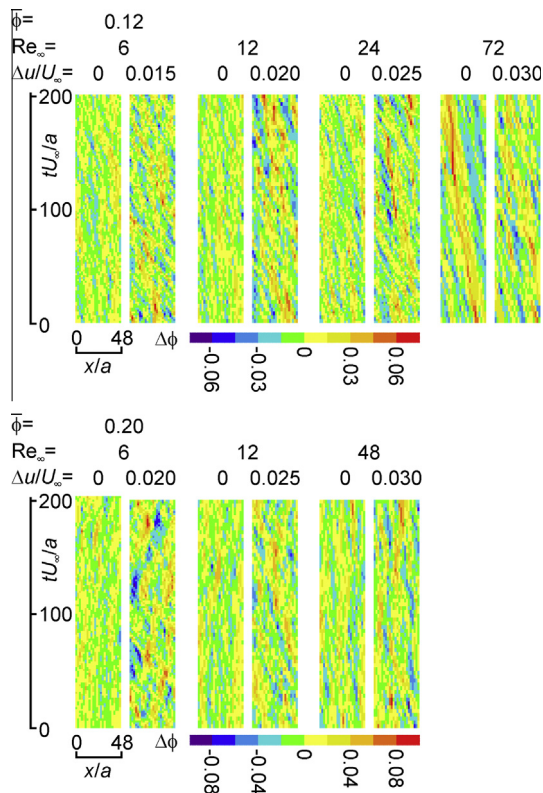


Fig. 13. Space-time plots of the solids volume fraction. Comparison between cases as identified in Fig. 12 that have approximately the same $\frac{F}{\langle n_a \rangle_{\Delta u=0}}$ but different $F_{\Delta u=0}$. For each aggregating case we compare with the corresponding case that has $\Delta u = 0$.

The effects of the spatial resolution of the simulations were examined and found to be small. Also the consequences of having finite size domains were assessed. In a few respects this is an important issue. In the first place given correlation lengths effects in settling suspensions, in the second place because aggregates can grow to a priori unknown sizes so that an assessment of domain size over primary particle size is not sufficient. The average drag appeared insensitive to domain size in the investigated range. This may be different for fluctuating drag; we will leave this issue for future work. Also the aggregation process – including its transients – were found to be independent of domain size up to $\bar{\phi} = 0.25$. For denser suspensions ($\bar{\phi} = 0.32$ as an example) and relatively strong interaction potentials, aggregates of a size comparable to the size of the domain were sometimes produced and in such cases a steady state was not reached. These cases have been discarded in further analysis since they suffer from unphysical self-interaction through the periodic boundaries.

The average drag as observed in settling, non-aggregating suspensions qualitatively behaved as expected based on previous studies in the literature. In a quantitative sense it clearly differed from drag in static, random sphere assemblies. We showed that the topology of a settling suspension is not random and that this has consequences for the drag force. Also the motion of the particles relative to one another adds to the average drag experienced by the spheres.

Settling rates clearly increase if the particles aggregate. These increased rates have been interpreted in terms of per-sphere drag reduction. For given overall solids volume fraction, the per-sphere drag reduction mainly depends on the strength of the interaction potential and on the level of inertia present in the system (as a metric for the latter the single-sphere settling Reynolds number Re_∞ was chosen). The effect of inertia could be traced back to the aggregate sizes that are much smaller for higher Re_∞ as a result of enhanced collision rates and liquid deformations that destabilize large aggregates. There is, however, no universal relation between aggregate size and drag reduction. One reason is that the attraction between the primary particles not only brings about aggregation; it also generates larger scale inhomogeneity in the suspension and does so differently for different Reynolds numbers. In denser systems larger aggregates are formed if the same attractive interaction strength is applied. This does, however, not mean that drag is more strongly reduced in the denser systems.

Future work will focus on a better understanding and more universal ways to describe and possibly predict enhanced settling as a result of aggregation. In addition, the sensitivity of the results with respect to the specifics of the interaction potential needs to be tested. A way to approach this is to mimic experimentally observed interaction potentials and simulate systems that are amenable to experimental testing.

From a more practical standpoint we plan to include the transport of a flocculant (an agent that stimulates aggregation, e.g. a polymer) and make the interaction potential dependent on its local concentration. In dense suspensions, the spreading of a scalar through the liquid phase poses a significant mixing problem and potentially is a rate limiting step in large scale flocculation processes.

References

Bartels, M., Lin, W., Nijenhuis, J., Kapteijn, F., Van Ommen, J.R., 2008. Agglomeration in fluidized beds at high temperatures: Mechanisms, detection and prevention. *Energy Fuels* 23, 157–169.
 Batchelor, G.K., 1972. Sedimentation in a dilute dispersion of spheres. *J. Fluid Mech.* 52, 245–268.
 Beetstra, R., Van der Hoef, M.A., Kuipers, J.A.M., 2007. Drag force of intermediate Reynolds number flows past mono- and bidisperse arrays of spheres. *AIChE J.* 53, 489–501.

come very close, and a hydrodynamic radius calibration was applied to account for artifacts related to representing spherical surfaces on a cubic lattice.

- Bouyer, D., Liné, A., Do-Quang, Z., 2004. Experimental analysis of floc size distribution under different hydrodynamics in a mixing tank. *AIChE J.* 50, 2064–2081.
- Brady, J.F., Bossis, G., 1988. Stokesian dynamics. *Annu. Rev. Fluid Mech.* 20, 111–157.
- Chen, S., Doolen, G.D., 1998. Lattice-Boltzmann method for fluid flows. *Annu. Rev. Fluid Mech.* 30, 329–364.
- Derksen, J.J., 2012. Direct numerical simulations of aggregation of monosized spherical particles in homogeneous isotropic turbulence. *AIChE J.* 58, 2589–2600.
- Derksen, J.J., Eskin, D., 2010. Potential of micro-channel flow for agglomerate breakage. *Ind. Eng. Chem. Res.* 49, 10633–10640.
- Derksen, J.J., Sundaresan, S., 2007. Direct numerical simulations of dense suspensions: wave instabilities in liquid-fluidized beds. *J. Fluid Mech.* 587, 303–336.
- Duru, P., Nicolas, M., Hinch, J., Guazzelli, É., 2002. Constitutive laws in liquid-fluidized beds. *J. Fluid Mech.* 452, 371–404.
- Eggels, J.G.M., Somers, J.A., 1995. Numerical simulation of free convective flow using the lattice-Boltzmann scheme. *Int. J. Heat Fluid Flow* 16, 357–364.
- Ernst, M., Dietzel, M., Sommerfeld, M., 2013. A Lattice-Boltzmann method for simulating transport and agglomeration of resolved particles. *Acta Mechanica*, in press. <http://dx.doi.org/10.1007/s00707-013-0923-1>.
- Flesch, J.C., Spicer, P.T., Pratsinis, S.E., 1999. Laminar and turbulent shear-induced flocculation of fractal aggregates. *AIChE J.* 45, 1114–1124.
- Goldstein, D., Handler, R., Sirovich, L., 1993. Modeling a no-slip flow boundary with an external force field. *J. Comp. Phys.* 105, 354–366.
- Guazzelli, É., 2001. Evolution of particle-velocity correlations in sedimentation. *Phys. Fluids* 13, 1537–1544.
- Guazzelli, É., Hinch, J., 2011. Fluctuations and instability in sedimentation. *Annu. Rev. Fluid Mech.* 43, 97–116.
- Harshe, Y.M., Lattuada, M., Soos, M., 2011. Experimental and modeling study of breakage and restructuring of open and dense colloidal aggregates. *Langmuir* 27, 5739–5752.
- Hasimoto, H., 1959. On the periodic fundamental solutions of the Stokes equations and their application to viscous flow past a cubic array of spheres. *J. Fluid Mech.* 5, 317–328.
- Hill, R.J., Koch, D.L., Ladd, A.J.C., 2001. Moderate-Reynolds-number flows in ordered and random arrays of spheres. *J. Fluid Mech.* 448, 243–278.
- Kandhai, D., Derksen, J.J., Van den Akker, H.E.A., 2003. Interphase drag coefficients in gas–solid flows. *AIChE J.* 49, 1060–1065.
- Kim, S., Karrila, S.J., 1991. *Microhydrodynamics: Principles and Selected Applications*. Butterworth-Heinemann, Boston.
- Ladd, A.J.C., 1994. Numerical simulations of particle suspensions via a discretized Boltzmann equation. Part I: Theoretical Foundation. *J. Fluid Mech.* 271, 285–309.
- Ladd, A.J.C., 2002. Effect of container walls on the velocity fluctuations of sedimenting spheres. *Phys. Rev. Lett.* 88, 048301.
- Lucci, F., Ferrante, A., Elghobashi, S., 2010. Modulation of isotropic turbulence by particles of Taylor length-scale size. *J. Fluid Mech.* 650, 5–55.
- Mucha, P.J., Tee, S.-Y., Weitz, D.A., Shraiman, B.I., Brenner, M.P., 2004. A model for velocity fluctuations in sedimentation. *J. Fluid Mech.* 501, 71–104.
- Nguyen, N.-Q., Ladd, A.J.C., 2002. Lubrication corrections for lattice-Boltzmann simulations of particle suspensions. *Phys. Rev. E* 66, 046708.
- Nguyen, N.-Q., Ladd, A.J.C., 2005. Sedimentation of hard-sphere suspensions at low Reynolds number. *J. Fluid Mech.* 525, 73–104.
- Richardson, J.F., Zaki, W.N., 1954a. Sedimentation and fluidisation: part 1. *Trans. Instn. Chem. Engrs.* 32, 35–53.
- Richardson, J.F., Zaki, W.N., 1954b. The sedimentation of a suspension of uniform spheres under conditions of viscous flow. *Chem. Eng. Sci.* 8, 65–73.
- Saffman, P.G., 1973. On the settling of free and fixed suspensions. *Studies Appl. Math.* 52, 115–127.
- Sangani, A.S., Acrivos, A., 1982. Slow flow through a periodic array of spheres. *Int. J. Multiphase Flow* 8, 343–360.
- Schiller, L., Naumann, A., 1933. *Über die grundlegenden Berechnungen bei der Schwerkraftaufbereitung*. *Ver. Deut. Ing. Z.* 77, 318–320.
- Smith, S.W., Hall, C.K., Freeman, D.B., 1997. Molecular dynamics for polymeric fluids using discontinuous potentials. *J. Comp. Phys.* 134, 16–30.
- Snabre, P., Pouligny, B., Metayer, C., Nadal, F., 2009. Size segregation and particle velocity fluctuations in settling concentrated suspensions. *Rheol. Acta* 48, 855–870.
- Somers, J.A., 1993. Direct simulation of fluid flow with cellular automata and the lattice-Boltzmann equation. *Appl. Sci. Res.* 51, 127–133.
- Stokes, G.G., 1901. *Mathematical and Physical Papers, Volumes I-V*. Cambridge University Press, Cambridge.
- Succi, S., 2001. *The lattice Boltzmann equation for fluid dynamics and beyond*. Clarendon Press, Oxford.
- Ten Cate, A., Nieuwstadt, C.H., Derksen, J.J., Van den Akker, H.E.A., 2002. PIV experiments and lattice-Boltzmann simulations on a single sphere settling under gravity. *Phys. Fluids* 14, 4012–4025.
- Ten Cate, A., Derksen, J.J., Portela, L.M., Van den Akker, H.E.A., 2004. Fully resolved simulations of colliding spheres in forced isotropic turbulence. *J. Fluid Mech.* 519, 233–271.
- Van der Hoef, M.A., Beetstra, R., Kuipers, J.A.M., 2005. Lattice-Boltzmann simulations of low-Reynolds-number flow past mono- and bidisperse arrays of spheres: results for the permeability and drag force. *J. Fluid Mech.* 528, 233–254.
- Verlet, L., Weis, J.-J., 1972. Equilibrium theory of simple liquids. *Phys. Rev. A* 5, 939–952.
- Wang, X., Feng, X., Xu, Z., Masliyah, J.H., 2010. Polymer aids for settling and filtration of oil sands tailings. *Can. J. Chem. Eng.* 88, 403–410.
- Wylie, J.J., Koch, D.L., Ladd, A.J.C., 2003. Rheology of suspensions with high particle inertia and moderate fluid inertia. *J. Fluid Mech.* 480, 95–118.
- Yamamoto, Y., Potthoff, M., Tanaka, T., Kajishima, T., Tsuji, Y., 2001. Large-eddy simulation of turbulent gas-particle flow in a vertical channel: effect of considering inter-particle collisions. *J. Fluid Mech.* 442, 303–334.
- Yin, X., Sundaresan, S., 2009. Drag law for bidisperse gas–solid suspensions containing equally sized spheres. *Ind. Eng. Chem. Res.* 48, 227–241.